RESEARCH ARTICLE

Overmodulation of Six-Phase Cascaded-CSI Using Optimal Harmonics Injection

AHMED SALEM[1], **(Graduate Student Member, IEEE),**
AND MEHDI NARIMANI[2], **(Senior Member, IEEE)**
[1]Department of Electrical Engineering, Alexandria University, Alexandria 21544, Egypt
[2]Department of Electrical and Computer Engineering, McMaster University, Hamilton, ON L8S 4L8, Canada

Corresponding author: Ahmed Salem (Ahmed_salem@alexu.edu.eg)

ABSTRACT This paper proposes a new and straightforward method to extend the modulation range of the six-phase cascaded current source inverter (CSI). The proposed technique employs vector space decomposition (VSD) to mitigate the inverter current harmonics and extend the linear modulation region by about 8%. For motor drive applications, increasing the fundamental output component can reflect higher torque production capability for the same drive size, given that thermal limits are not exceeded. The extension can be realized by injecting optimized xy harmonics while keeping the amplitude of the resulting phase currents under the maximum value. The method utilizes a look-up table of optimized values of the injected harmonics to extend the modulation range. The output filter capacitor effects are also studied in this paper, and a selection approach is introduced. Finally, the experimental results of a C-CSI laboratory prototype are presented and discussed to verify the feasibility of the proposed modulation technique.

I. INTRODUCTION

Current-source inverter (CSI) is one of the attractive candidates for medium-voltage high-power motor drive applications [1] due to its tolerance for short-circuit faults compared to voltage-source inverters (VSI). For instance, an offshore wind farm with high-voltage DC transmission (HVDC) based on the CSI topology has been discussed [2], [3]. Other industrial applications such as aerospace applications [4], electric vehicle applications [5], [6], [7], [8], and industrial motor drives [9] are prominent candidates for using CSI technology as well. In addition to fault-tolerance, another advantage of CSI is the mitigation of the dv/dt problem that occurs at switching transitions. This can help to avoid the deterioration of the bearing of motors, failure in the insulation of the wiring, and high acoustic noise while operating [10]. The output voltages and currents of a CSI are motor-friendly, thanks to

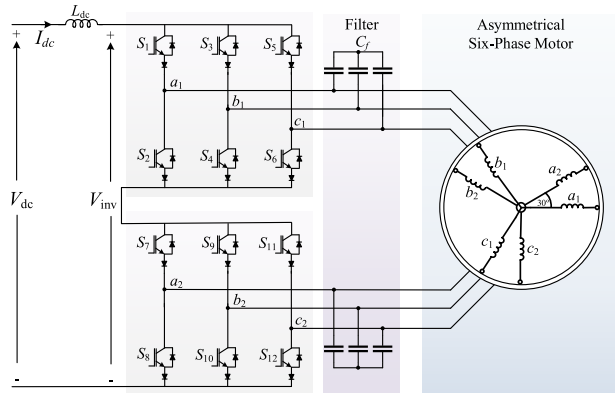The associate editor coordinating the review of this manuscript and approving it for publication was Qinfen Lu.

the capacitive filtering stage. The bulky dc-link electrolytic capacitor banks are also removed in CSIs, which can help to improve the reliability of the overall system [11]. Moreover, CSI can control the output phase currents directly without the need to control the output voltages to produce the reference currents [12].

Multiphase drives have great potential for several industry applications [13], [14], such as electric ship propulsion [15], more electric aircraft [16], and high-power traction applications [17]. Six-phase systems are prevalent among multiphase systems for their inherent two three-phase structure. Distinctive features arise from the change of the displacement angle between the two three-phase winding sets in six-phase drives. The arrangement with a 30° phase shift is called the asymmetrical six-phase or dual three-phase machine. In contrast, a displacement of 60° results in a symmetrical six-phase system. The symmetrical machines outmatch the asymmetrical ones in the post-fault torque range [18]. However, asymmetrical machines have a better distribution of airgap magneto force

(MMF) [19]. Hence the latter is considered in this context. If the phases are connected in a star-shaped connection, every three-phase group set will have a neutral point, and they can be either connected to form a single-neutral point (1N) or disconnected from each other and form two-isolated neutral points (2N).

For a CSI-based six-phase system, a cascaded CSI (C-CSI) topology is introduced in [20] and shown in Fig. 1. The cascaded connection of the two three-phase CSIs is implemented to simultaneously supply each group set of the load. Another configuration of the six-phase CSI can be achieved by connecting the two three-phase CSIs in parallel (P-CSI). However, only one three-phase CSI is allowed to work at a time in P-CSI [20]. The main advantage of the C-CSI topology is the capability to double the dc-link current utilization compared to P-CSI because both three-phase inverters can operate simultaneously. For modeling, a six-phase system can be considered a double three-phase system called the *double-dq* method. In this method, the variables of each group set can be transferred to a three-dimensional space; two axes represent an equivalent in-quadrature two-phase system, and the third one represents one zero-sequence axis. The C-CSI modulation technique [20] is based on the *double-dq* modeling method. However, the most used method to simplify modeling a multiphase system is the vector space decomposition (VSD) introduced in [21] and well-established for VSIs.

The development of space vector modulation (SVM) techniques to utilize the features of such systems is one of the attractive research topics in multiphase inverters. Using VSD modeling, the SVM method can control the harmonics in different subspaces [22], [23], [24]. Ordinarily, reducing the harmonics is the main target of most techniques to increase the system's efficiency and maintain thermal limits [25].

Moreover, in two-level VSI multiphase inverters, the modulation range can be extended linearly using the additional degrees of freedom [26], [27]. The penalty of such a feature is the increased harmonic content in the output voltage waveform, which implicates increased losses and lower efficiency. This topic is exciting since the trade-off can

achieve beneficial gains outweighing the drawbacks by optimizing the harmonic content required to achieve the extension. This approach has been investigated for five-phase systems [28] and six-phase ones [29], [30], [31]. In these methods, an objective function is defined based on the harmonic content in the extra subspaces, and the optimization process aims to achieve the desired modulation index in the fundamental subplane with the minimum possible harmonic content in the other subplanes.

The SVM based on the VSD method has been discussed for five-phase CSI [11], [32]. In both works, an extension method of the dc-link current utilization is achieved by using the same ratio between the large and medium vectors in [32] or injecting a third harmonic component in the additional subspace [11]. C-CSI modulation has been discussed in [20] based on the *double-dq* method. However, to the best of the authors' knowledge, a realization of SVM based on VSD for C-CSI and extension of dc-link utilization has not been investigated. In this paper, the VSD modeling method is proposed and developed for asymmetrical six-phase C-CSI to offer:

- The proposed method adopts the two large two medium vectors modulation scheme to control the modulation index linearly from zero to the maximum. Minimized harmonic content is achieved using zero-average Ampere-second balance per switching sampling period by using the VSI and CSI systems analogy.
- Extension of the modulation index range by around 8% with minimum injected harmonics in the *xy* using a new proposed approach based on stored, operating points in a look-up table (LUT) for fast and easy implementation of the scheme.

The work presented in this paper is distinguished from the VSD-based for VSIs in devising the modulation in the extension region. In the proposed method, a backward approach is developed. The desired output after harmonic injection is shaped, and the ability of C-CSI is checked to produce such a reference. Then, the operating points are stored in a LUT to recall while needed to achieve a desired modulation index in the extension range. On the contrary, in the previous methods for VSI, the possible inverter states are studied in the extension region, and the schemes are based on optimizing all the possible solutions based on the geometry of the selected vectors. The proposed method can also be generalized easily to other multiphase CSIs based on each case's available degrees of freedom. Another advantage of the proposed method is that the dwell time calculation remains the same over the whole modulation range, unlike the previous extension works for VSIs. The proposal mimics the harmonic injection methods used for torque density improvement, such as in [33], [34], only using SVM rather than tuning several proportional-resonant controllers as in VSI-based systems.

This paper is organized as follows: Section II discusses the system model, and the inverter outputs are mapped into the equivalent subspaces using the VSD method. The details of

TABLE 1. Categories of current vectors based on the states of C-CSI.

Group	Quantity	Color
I_L	$(\sqrt{3}+1)I_{dc}/\sqrt{2}$	——— (red)
I_{M1}	$(\sqrt{2})I_{dc}$	——— (purple)
I_{M2}	I_{dc}	——— (blue)
I_S	$(\sqrt{3}-1)I_{dc}/\sqrt{2}$	——— (green)

the proposed SVM technique are illustrated in Section III, and the optimization problem is to minimize the harmonics content while realizing the maximum linear modulation index. The effects of the filtering capacitors are also discussed in this section. The experimental results with discussions are presented in Section V.

II. MODELING OF A SIX-PHASE C-CSI

A. OPERATION OF A SIX-PHASE C-CSI

The structure of a six-phase cascaded CSI is shown in Fig. 1. The C-CSI comprises two three-phase CSIs connected in series. The dc-link current I_{dc} passes from one inverter to the other one, as shown in Fig. 1. This structure allows the modulation of the two inverters separately, which means full utilization of the dc-link current.

Two conditions of operation must be followed to operate CSIs properly. The first condition is that the I_{dc} must be continuous without any interruption. The second condition is to produce a predefined output current waveform. This condition allows only two out of the six switches to be turned on simultaneously in each three-phase inverter. It should be noted that the only valid neutral point configuration that can be applied here is the 2N configuration. There are nine possible switching states for each three-phase CSI [33], [34], and thus in total, there are 81 possible switching states for the six-phase C-CSI. The output currents produced by the possible switching state can be calculated using (1):

where T_s is the switching period. t_1 to t_4 are the dwell times of the selected active vectors per sector I_1 to I_4, respectively. In Eq. TABLE 1 the current components I_g^γ, $\gamma \in \{\alpha, \beta, x, y\}$ refers to the axis of synthetization of the component, and $g \in \{1, 2, 3, 4\}$ refers to the order of the selected vector to represent a sector of modulation. Meanwhile i_r^γ refers to the decoupled reference current components.

$$\begin{bmatrix} i_{a1} \\ i_{b1} \\ i_{c1} \\ i_{a2} \\ i_{b2} \\ i_{c2} \end{bmatrix} = \begin{bmatrix} S_1 - S_2 \\ S_3 - S_4 \\ S_5 - S_6 \\ S_7 - S_8 \\ S_9 - S_{10} \\ S_{11} - S_{12} \end{bmatrix} I_{dc} \quad (1)$$

where S_j, j= {1, 2, …12} is the state of the inverter switch and i_{a1} to i_{c2} are the phase currents.

B. VECTOR SPACE DECOMPOSITION (VSD)

The VSD method decomposes machine variables (voltage, current, and flux) into three two-dimensional subspaces. The three subspaces are orthogonal to each other; hence decoupled variables are mapped to each subspace. The first subspace is called the $\alpha\beta$ subspace. As in the Clarke transformation, the $\alpha\beta$ subspace represents all the harmonics of the order $l = 12h \pm 1$, $h = (1, 2, 3, \ldots)$ which impact the electromechanical conversion process (i.e., torque-producing harmonics). The second subspace is called xy subspace, and harmonics of the order $l = 6h\pm1$, $h = (1, 3, 5, \ldots)$ are mapped to it and considered as loss components. The final subspace is the representation of the triplen harmonics or the zero-sequence harmonics $l = 3h$, $h = (1, 3, 5, \ldots)$ and is referred to as the 0_+0_- subspace. The xy and the 0_+0_- subspaces do not contribute to the torque production process, and they are losses harmonics.

A transformation matrix is deduced mathematically in [21] to transfer six-phase currents into the three subspaces. This transformation is based on the phase shift angle between the two-three phase group sets and the angles between the phases in each group and is given in (2):

$$\begin{bmatrix} i_\alpha \\ i_\beta \\ i_x \\ i_y \\ i_{0+} \\ i_{0-} \end{bmatrix} = \frac{1}{\sqrt{3}} \begin{bmatrix} 1 & -\frac{1}{2} & -\frac{1}{2} & \frac{\sqrt{3}}{2} & -\frac{\sqrt{3}}{2} & 0 \\ 0 & \frac{\sqrt{3}}{2} & -\frac{\sqrt{3}}{2} & \frac{1}{2} & \frac{1}{2} & -1 \\ 1 & -\frac{1}{2} & -\frac{1}{2} & -\frac{\sqrt{3}}{2} & \frac{\sqrt{3}}{2} & 0 \\ 0 & -\frac{\sqrt{3}}{2} & \frac{\sqrt{3}}{2} & \frac{1}{2} & \frac{1}{2} & -1 \\ 1 & 1 & 1 & 0 & 0 & 0 \\ 0 & 0 & 0 & 1 & 1 & 1 \end{bmatrix} \begin{bmatrix} i_{a1} \\ i_{b1} \\ i_{c1} \\ i_{a2} \\ i_{b2} \\ i_{c2} \end{bmatrix} \quad (2)$$

The new variables are decoupled and can be controlled to achieve the desired performance, such as desired power transfer and power factor control for grid-tied applications or the torque-speed references for motor drive applications.

C. MAPPING OF THE CURRENT COMPONENTS

The VSD method can help to map the output current vectors into the three-decoupled subspaces using all the possible switching states. Since the load is connected in the 2N configuration, the current components in the 0_+0_- subspace are all nullified. The current components are shown in Fig. 2. These output currents components are the result of applying all possible switching states and can be determined by using Eq. (1) and (2). Each vector is referred to as I_p as $p \in \{1, 2, .., 81\}$.

The mapped components are classified in this context based on their magnitude in the $\alpha\beta$ subspace, shown in

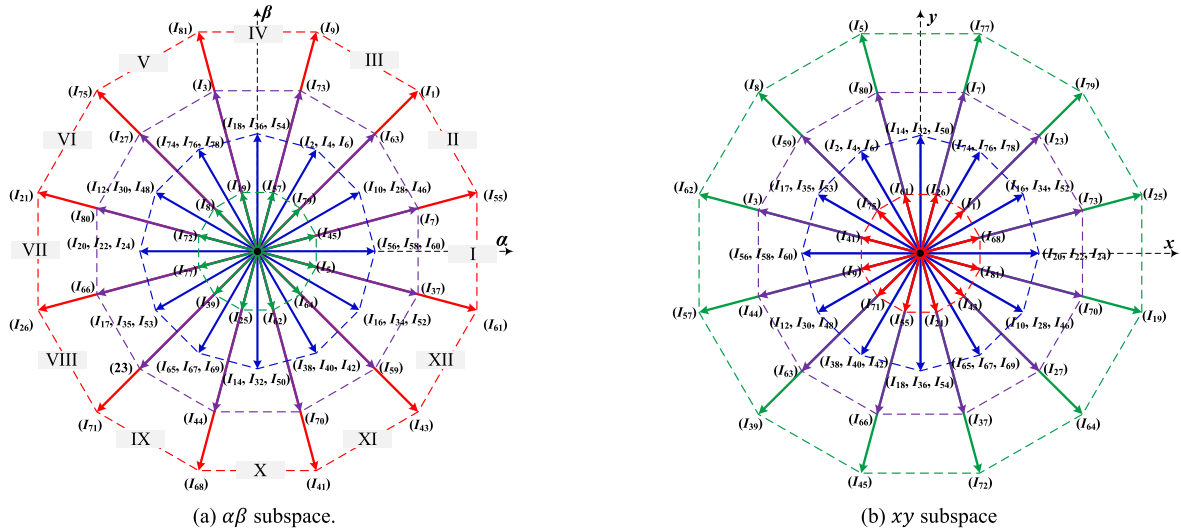(a) $\alpha\beta$ subspace.

(b) xy subspace

FIGURE 2. Projection of possible output states of the C-CSI structure using the VSD method.

TABLE 1. The group I_L has the largest $\alpha\beta$ components and the smallest xy components. The classified components as I_{M1} have equal magnitudes in both $\alpha\beta$ and the xy subspaces. It is worth noting that the two groups I_L and I_{M1} have components that are out of phase in the xy subspace, which can be exploited in the modulation scheme. The vectors from the other groups have lower magnitudes compared to the others.

III. THE PROPOSED MODULATION TECHNIQUE

In this paper, the proposed approach introduces two regions for the modulation index. The first region (Region I) covers from zero to the highest modulation index. In this region, the VSD-based SVM technique is employed to diminish the unwanted xy harmonics and obtain sinusoidal output currents. The second region (Region II) is the extension region, in which the proposed method is applied to achieve the highest possible modulation index (1.08) while minimizing harmonic components.

A. PROPOSED VSD-BASEDt SVM TECHNIQUE FOR C-CSI

The $\alpha\beta$ subspace can be divided into twelve sectors. The numbering of the sectors is shown from I to XII in Fig. 2(a). When a reference vector is in each sector, the reference vector can be synthesized by selecting four active vectors and one null vector. In the proposed approach, a five-segment switching sequence cycle is also considered. The method is based on the analogy between VSI and CSI. Hence, two vectors are chosen from the large group (I_L), and the other two vectors are chosen from the (I_{M1}) group as in [31]. The large and medium vectors are selected such that each large vector is in the same direction as the medium vector in the $\alpha\beta$ subspace. Meanwhile, they are out of phase in the xy subspace. One example in Sector I is shown in Fig. 3.

The calculation of the dwell times is given TABLE 1 in the same manner as the six-phase VSI [35]. The calculation
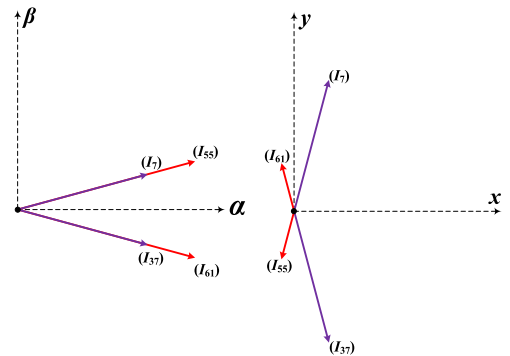

FIGURE 3. The selected vectors for sector I.

method is based on synthesizing the selected vectors and the reference into their respective α, β, x, y components:

$$\begin{bmatrix} t_1 \\ t_2 \\ t_3 \\ t_4 \\ t_0 \end{bmatrix} = \underbrace{\begin{bmatrix} I_1^\alpha & I_2^\alpha & I_3^\alpha & I_4^\alpha & 0 \\ I_1^\beta & I_2^\beta & I_3^\beta & I_4^\beta & 0 \\ I_1^x & I_2^x & I_3^x & I_4^x & 0 \\ I_1^y & I_2^y & I_3^y & I_4^y & 0 \\ 1 & 1 & 1 & 1 & 1 \end{bmatrix}^{-1}}_{c} \begin{bmatrix} i_r^\alpha \\ i_r^\beta \\ i_r^x \\ i_r^y \\ 1 \end{bmatrix} T_s \quad (3)$$

Since the aim of this paper is to apply VSD modeling to extend the maximum modulation index in C-CSI, only vectors from the I_L and I_{M1} groups are considered in the following discussions.

B. REGIONS OF OPERATION

Two regions of operation for the proposed scheme are defined and studied. This categorization is based on the designated level of harmonics allowed in the output currents of the C-CSI. The following subsections define the set limits of the output harmonics for each region, and it is explained how to modulate the scheme accordingly:

1) REGION I (MINIMUM HARMONICS REGION)

Undoubtedly, lower harmonic content in the output current can lead to higher efficiency and better system thermal performance. However, the harmonics could contribute to the output power or torque production [36], [37]. In Region I, the goal is to linearly change the modulation range from zero to maximum with the low content of the xy subplane harmonics. This can be done by setting the references i_r^x, i_r^y to zero in the dwell times calculations in Eq. TABLE 1.

The modulation index (m) is defined as the ratio between the amplitude of the fundamental component of the reference inverter currents $\left|i_{f1,max}^{inv}\right|$ and the dc-link current I_{dc}. Hence, the six-phase reference currents vector, i_r^{inv} can be realized using Eq. (4):

$$\left[i_r^{inv}\right] = \begin{bmatrix} i_{a1} \\ i_{b1} \\ i_{c1} \\ i_{a2} \\ i_{b2} \\ i_{c2} \end{bmatrix} = mI_{dc} \begin{bmatrix} \cos(\theta) \\ \cos(\theta - 120°) \\ \cos(\theta - 240°) \\ \cos(\theta - 30°) \\ \cos(\theta - 150°) \\ \cos(\theta - 270°) \end{bmatrix} \quad (4)$$

Based on the fundamentals of pulse width modulation, as the modulation index increases, the null time decreases. Hence, the maximum modulation index in Region I $\left(m_{max}^{Reg.I}\right)$ can be determined by determining the equation to calculate the null time (t_o). Since the dwell times of the inverter are periodically repeated in every sector, studying one sector of modulation is enough to calculate t_0.

For instance, the following procedure obtains the null time equation in sector I. To determine the t_0 first, all the components on the right-hand side in TABLE 1 must be defined. The components I_g^γ of the selected active vectors ($I_{61}, I_{37}, I_7, I_{55}$) in sector I should be substituted in (3).

Then, by using the VSD transformation given in (2), the reference currents can be mapped into the decoupled reference current components i_r^γ shown in (5):

$$\begin{cases} i_r^\alpha = \sqrt{3}\, mI_{dc} \cos(\theta) \\ i_r^\beta = \sqrt{3}\, mI_{dc} \sin(\theta) \\ i_r^x = i_r^y = 0 \\ i_r^{0+} = i_r^{0-} = 0 \end{cases} \quad (5)$$

The 0_+0_- References are physically realized because of the neutral connection applied in the C-CSI. Consequently, there is no need to include the last branch of Eq. (5) in the following calculations. The reference output currents i_r^γ given in (5) should be substituted in TABLE 1 to determine the null time equation in sector I, and it is described in (6).

$$t_{0,\text{sectorI}} = T_s \left(1 - m \cos(\theta)\right) \quad (6)$$

To achieve $m_{max}^{Reg.I}$, two variables in Eq. (6) must be determined; the values of θ and $t_{0,\text{sectorI}}$. The angle that represents the minimum null time value is $\theta = 0°$ which makes the cosine term in Eq. (6) becomes maximum. By substituting
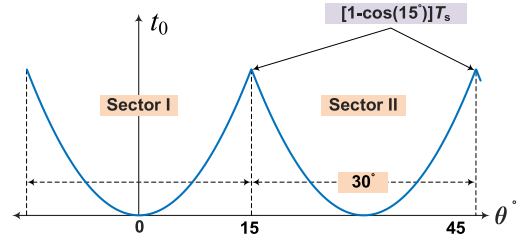

FIGURE 4. Null time at the maximum modulation index.

for θ, Eq. (6) becomes as III-B2.

$$(t_{0,\text{sectorI}})_{min}\big|_{\theta=0} = T_s \left(1 - \left(m_{max}^{Reg.I}\right)\right) \quad (7)$$

The null time $t_{0,\text{sectorI}}$ at $m_{max}^{Reg.I}$ reaches zero, which is the minimum realizable null time. By equating III-B2 to zero, the $m_{max}^{Reg.I}$ deduced is equal to one. That means the ability of the six-phase C-CSI to realize the maximum fundamental output currents ($\left|i_{f1,max}^{inv}\right|$) with zero-average xy harmonic currents. Fig. 4 shows the null time over two sectors at the maximum modulation index inside Region I. It is worth mentioning that applying a zero-average Ampere balance does not guarantee the total elimination of the harmonic currents in the xy subplane. However, a minimized harmonic content can be achieved by using such a technique [21].

2) REGION II (EXTENDED REGION)

In Region II, the target of the proposed SVM is to take advantage of the C-CSI system and achieve the full dc-link utilization linearly. The proposal is to calculate and inject appropriate harmonic content in the xy to produce a higher fundamental component than Region I. The dwell time calculations in TABLE 1 can be used without changes. Unlike the triplen harmonics, the xy harmonics can flow without any hardware reconfiguration [38].

The harmonics mapped to the xy subspace are of the order $l = 6h \pm 1$, $h = (1, 3, 5, \ldots)$ as mentioned in the VSD section. The general formula of the output current waveform after injecting the xy harmonics is shown in (8):

$$i_o = I_{dc} \left[m\cos(\theta) + \left(\sum_{h=1,3,5,\ldots}^{\infty} k_{6h-1} \cos\left((6h-1)\theta + \varphi_{6h-1}\right) \right. \right.$$
$$\left. \left. + k_{6h+1} \cos\left((6h+1)\theta + \varphi_{6h+1}\right) \right) \right] \quad (8)$$

where k is the per-unit (p.u.) value of the injected harmonics and φ is the phase-shifting angles of the waveforms.

To obtain the form of the xy current components in the reference, every reference phase current in the reference vector $\left[i_r^{inv}\right]$ stated in (4) should be modified to include the injected currents as in (8). Then, by applying VSD transformation and simplifying the formulas, the current references injected in

the xy subspace are shown in (9):

$$\begin{bmatrix} i_r^x \\ i_r^y \\ i_r \end{bmatrix} = \sqrt{3} \, I_{dc} \sum_{h=1,3,5,\ldots}^{\infty} k_{6h-1} \begin{bmatrix} \cos\left((6h-1)\theta + \varphi_{6h-1}\right) \\ \sin\left((6h-1)\theta + \varphi_{6h-1}\right) \end{bmatrix}$$
$$+ k_{6h+1} \begin{bmatrix} \cos\left((6h+1)\theta + \varphi_{6h+1}\right) \\ -\sin\left((6h+1)\theta + \varphi_{6h+1}\right) \end{bmatrix} \qquad (9)$$

The next step is to determine the optimum values of the coefficients k. An optimization process is developed here to find these coefficients. The optimization aims to find the minimum harmonic content to be injected to extend the modulation range into Region II. The objective function (*obj*) is defined in (10), and it consists of the summation of the squared values of the coefficients. The optimization problem is to find the minimum of *obj* for each modulation index in Region II. The constraint is also illustrated in (11), representing the feasibility of applying the dwell times. These times calculated by TABLE 1 must be greater than or equal to zero at the values of k selected by the optimization process. The optimization problem can be solved using MATLAB software by deploying the fmincon() function with the MultiStart option.

$$obj = \sqrt{\sum_{h=1,3,5,\ldots}^{\infty} (k_{6h-1})^2 + (k_{6h+1})^2} \qquad (10)$$

$$\text{subjected to} [t_1 \ t_2 \ t_3 \ t_4 \ t_0]|_{\text{calculated at the selected} k's}$$
$$\geq [0 \ 0 \ 0 \ 0 \ 0] \qquad (11)$$

Since the formula in (9) is infinite, an algorithm is applied to determine a finite number of essential harmonics to get an applicable solution. The algorithm starts with $h = 1$ and attempts to solve the optimization with the modulation indexes beyond the limit of Region I. The optimization algorithm increases the values of m until no feasible solution can be found. This approach determines the maximum modulation index in Region II $\left(m_{max}^{Reg.II}\right)$ while applying a certain h. The algorithm stops at $h = 3$ and achieves $m_{max}^{Reg.II} = 1.0773$. The $h = 3$ means that the essential harmonics to be injected are the 5th, 7th, 17th, and 19th to ensure a feasible modulation. It is worth mentioning that considering cases with $h > 3$ would increase the accuracy of implementation and reduce the harmonic content. However, a trade-off is made to stop at $h = 3$ because of increased problems with higher harmonics regarding the implementation. The selection of the filtering capacitors and switching frequency are other motives to stop at $h = 3$. The optimum values of all coefficients are shown in Fig. 6 when the modulation index changes from 1 to 1.0773 in Region II.

As shown in Fig. 6, the amplitudes of the optimal injected harmonics are not linearly increasing with the modulation index in Region II. The SVM method can be easily implemented in Region II by storing the coefficients of the harmonics in the digital controller memory and recalling them when needed.
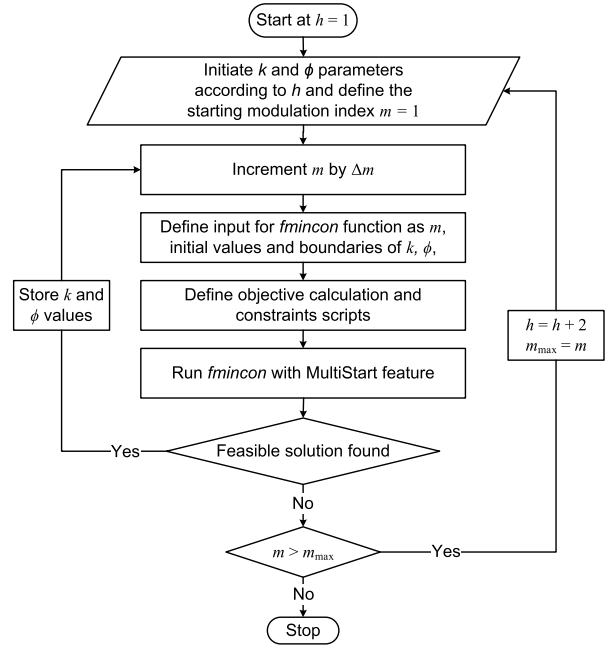

FIGURE 5. The flowchart of the optimization process to select the amplitudes and angles of the injected xy harmonics.
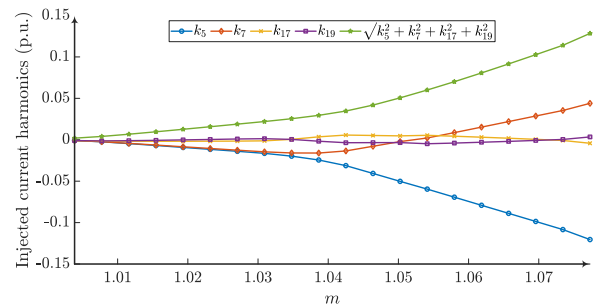

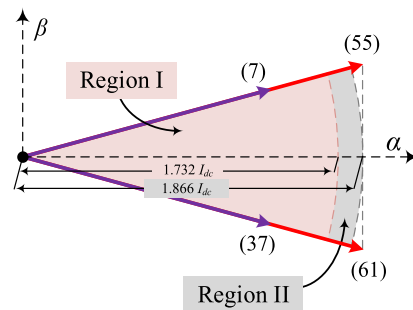**FIGURE 6.** The results of the optimization process with injection.

FIGURE 7. Feasible modulation regions.

Based on the deduced maximum modulation indexes in each region, the limits of the two regions can be illustrated geometrically in Fig. 7. The two arcs in Fig. 7 mark the end of the two regions. Region I realizes the references of magnitude up to $\sqrt{3} \, I_{dc}$. Region II ends at the outer circle with a perimeter equal to $1.0773\sqrt{3} \, I_{dc}$.

(a) Dwell times t_1, t_2 per T_s

(b) Dwell times t_3, t_4 per T_s

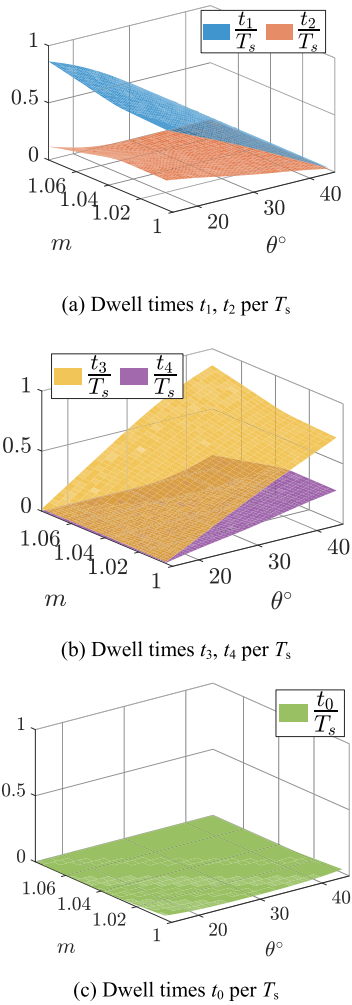(c) Dwell times t_0 per T_s

FIGURE 8. Dwell times as ratios of the sampling time over section **II** based on the optimized coefficients for the injected harmonics.

All the coefficients are calculated over the modulation range in Region II to check that the optimization problem results are feasible. Sector II is chosen to execute the check for feasibility since the dwell times are periodical, and one sector is enough for the check. The calculated dwell times are shown in Fig. 8. Since all the times are positive, it can be concluded that the C-CSI can realize the selected harmonics for injection.

C. EFFECT OF FILTERING CAPACITORS

A critical CSI output phenomenon is the resonance between the filtering capacitors and the load inductance. In this section, the per-phase equivalent circuit is studied to determine the relationship between the output current of the inverter I_{inv} and the load current I_{load} after the filtering stage, the main reason is to get a deeper understanding of the system to avoid the resonance effect. Another reason is to avoid amplifying or shifting the injected harmonics in the proposed extension method. The equivalent circuit of the filter capacitor and the load is shown in Fig. 9. The transfer function between the inverter output and the load in the s-domain is
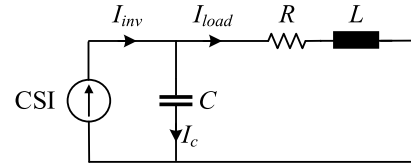

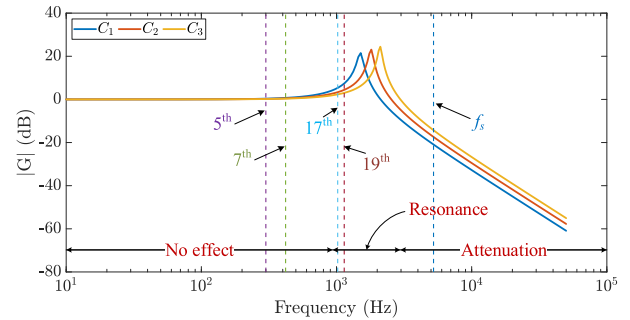**FIGURE 9.** Per-phase equivalent circuit of the load and filtering stages.

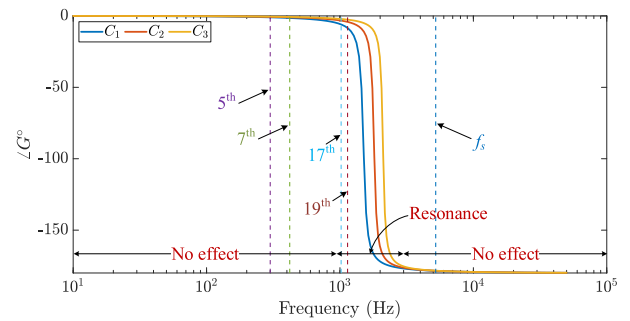**FIGURE 10.** Bode plot of the magnitude of the transfer function G.

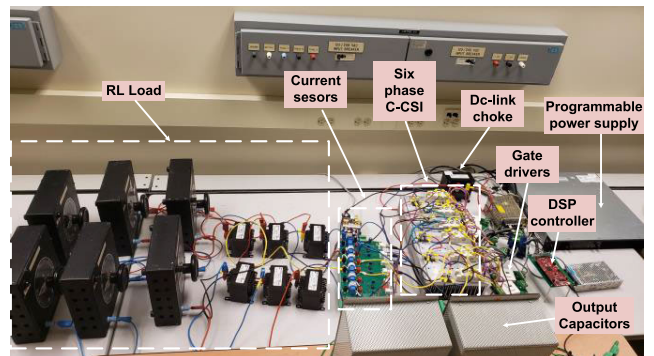**FIGURE 11.** The angle of the transfer function G.

FIGURE 12. The experimental setup to test the proposed scheme with R-L Load.

described in (12) for the case of $R - L$ loads. For steady state analysis, one can substitute $s = j\omega$ to get the magnitude and angle of the transfer function G to analyze the filtering stage:

$$G(s) = \frac{I_{load}}{I_{inv}} = \frac{1}{1 + RC.s + LC.s^2} \quad (12)$$

For discussion and clarification, a system running at the parameters specified in TABLE 2 is illustrated as an example. Given that the system under study is a medium-power

TABLE 2. Parameters of the resistive-inductive load for filter selection study.

Symbol	Parameter	Value
P_L	Rated power	250 kW
V	Rated voltage	210 V
f	Output frequency	60 Hz
f_s	Switching frequency	5 kHz
PF	Load power factor	0.9 lag
C_f	Filtering capacitor	30.7 μF

TABLE 3. Parameters of the experimental setup under study.

Symbol	Parameter	Value
I_{dc}	Dc-link current	2A
L_{dc}	Dc-link choke	70 mH
f	Output frequency	60 Hz
f_s	Switching frequency	4860 Hz
f_{sp}	Sampling frequency	48.6 kHz
$R-L$	Per-phase load	10 Ω - 10 mH
C_f	Filtering capacitor	1.6 μF

load, selecting the switching frequency of the CSI around the 5-10kHz range is suitable for such applications [5]. Using (13), three values of the filtering capacitor C_f are chosen such that the resonance frequency f_{res} would be at the (25th, 30th, 35th) harmonics.

$$C_f = \frac{1}{(2\pi f_{res})^2 L} \qquad (13)$$

The magnitude of G vs. a frequency range up to 50 kHz is presented in Fig. 10 using a bode plot. Meanwhile, the transfer function G angle is shown in Fig. 11. It can be noticed from Fig. 10 that the resonant frequency is at the selected harmonics, and the frequency span can be divided into three sections. The first one stretches from the beginning of the range of frequencies up to the resonance phenomenon. The second section is the resonance bandwidth, which is estimated at around 70.7% of the maximum value of |G|. The third section is the filtering section, where the high frequencies get attenuated, such as the band around the switching frequency. From Fig. 11, it can be deduced that the angles of the injected harmonics are barely changed, which makes the proposed SVM with the harmonic injection method more powerful to be used for C-CSI topology.

Selecting the filtering capacitor must ensure the following point based on the previous discussion. The f_{res} must be placed between the significant harmonics and the switching frequency harmonics. In addition, the high the value of f_{res}, leads to selecting small filtering capacitors, as seen in (13). This approach can reduce the size of capacitors and thus improve the system's overall lifetime. A simple solution to compensate for the filter effect on the magnitude and angle of the current is to employ an observer, which is introduced in [39] for motor drive applications.

IV. EXPERIMENTAL RESULTS
A. EXPERIMENTAL SETUP
A scaled-down prototype is used for the experimental test as illustrated in Fig. 12 to verify the feasibility of the proposed modulation scheme. The parameters of the experimental setup are summarized in TABLE 3. A six-phase C-CSI is implemented by six half-bridges SKM50GB12V IGBT modules connected to SKHI 22 A/B H4 gate drivers from Semikron. The reverse blocking is achieved by connecting

each half-bridge to a DSEI 2 × 31.06C diode module one diode to clamp each IGBT to the positive and negative rails.

The firing signals are generated by a LAUNCHXL-F28379D digital signal processor. A programmable dc supply is used in current-control mode to provide constant current. A six-phase load consisting of $R-L$ combination is used. The filtering capacitors are selected to place the f_{res} at the 13th harmonic. The fundamental frequency of the system is 60 Hz, and the setup runs at different modulation indexes in both modulation regions mentioned earlier.

B. EXPERIMENTAL RESULTS
The tests performed in this section include:
1) Running the inverter at $m = 1$.
2) Running the inverter at $m = 1.0773$.
3) A step change from $m = 0.8$ to $m = 1.0773$.
4) Comparison between the xy harmonic content (injected and measured) in the inverter output currents.

The experimental results of running the setup at $m= 1$ are shown in Fig. 13. This test shows the performance of the proposed scheme in Region I of the modulation. The waveforms shown are the load currents in Fig. 13(a) where phase currents (A_1, B_1, A_2, and B_2) appear on the 4-channel scope measured using hall-effect current sensors. The currents are sinusoidal and the harmonic spectrum of i_{A_1} is shown in Fig. 13(b) using the Fast Fourier Transform function in MATLAB. As expected, the spectrum shows low harmonic content as the operation is in Region I of the modulation.

The inverter output current is illustrated in Fig. 13(c) which also shows the dc-link current fed from the supply to the inverter which appears steady with small ripples. The spectrum of the inverter current is demonstrated in Fig. 13(d) and it is clear of harmonics since the xy harmonics are nullified in this region. The spectrum of the load and inverter currents are almost identical for the harmonics below the band of the switching frequency. This band of harmonics is diminished by the effect of the filtering capacitors. The load phase voltage is demonstrated in Fig. 13(e) and its spectrum is in Fig. 13(f). For R-L loads, the higher the harmonic understudy the higher the value of the reactance X_L, and the higher the voltage harmonic component that would appear. This is a drawback of using small filtering capacitors, however, this selection is necessary for operation in Region II.
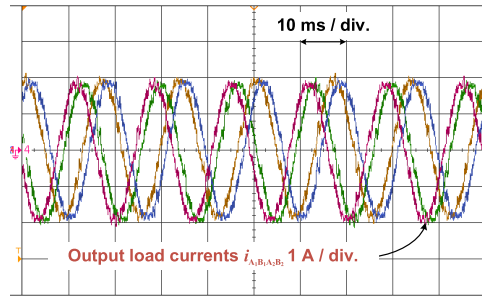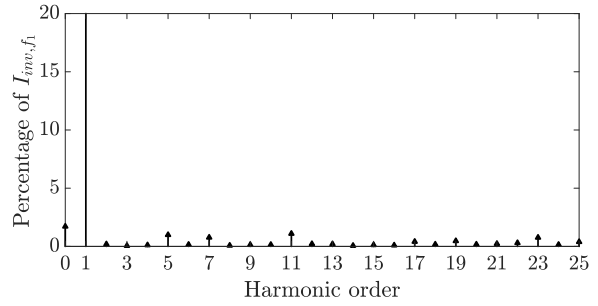
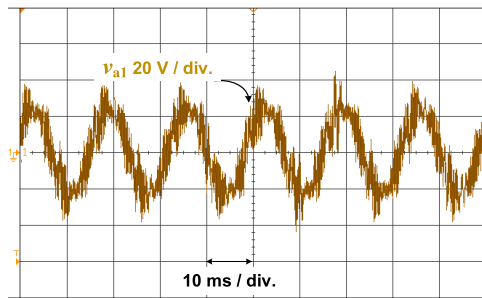(a) Load phase currents phases ($A_1, B_1, A_2,$ and B_2).
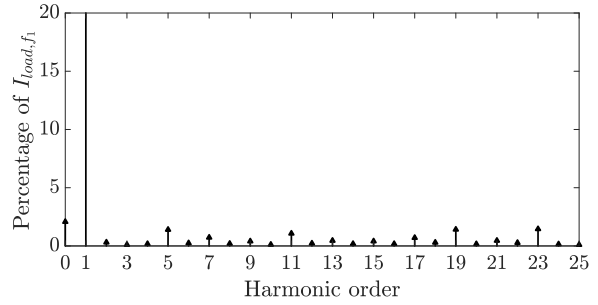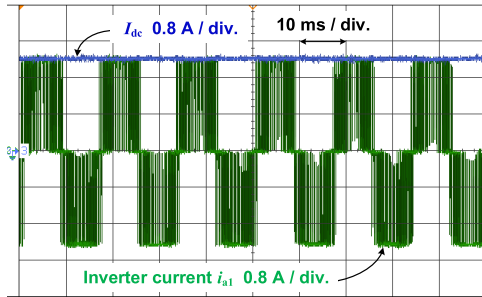
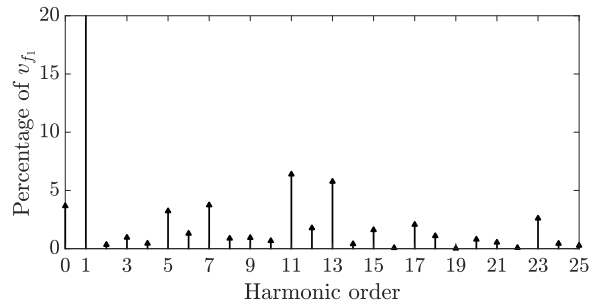(b) Harmonic spectrum of the load current.

(c) Inverter output current and the dc-link current.
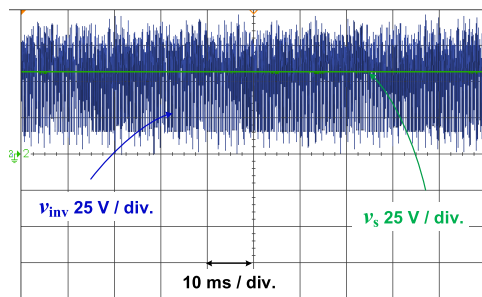

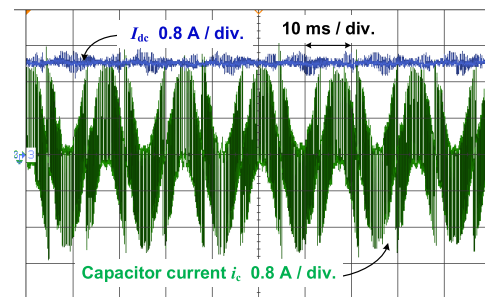(d) Harmonic spectrum of the inverter current.
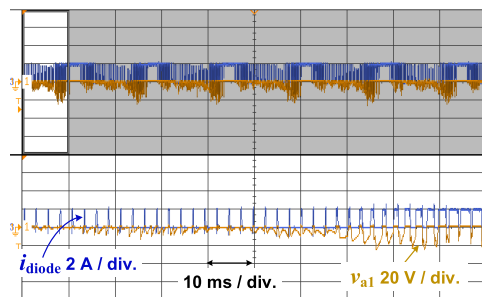

(e) Load phase voltage.

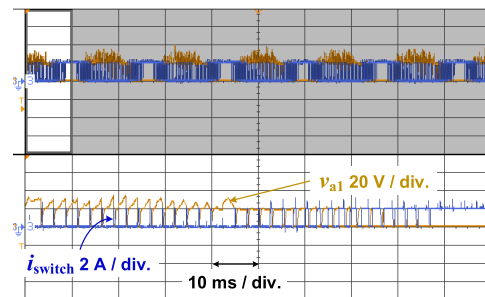(f) Harmonic spectrum of the load voltage.

(g) Dc-link and inverter input Voltages.
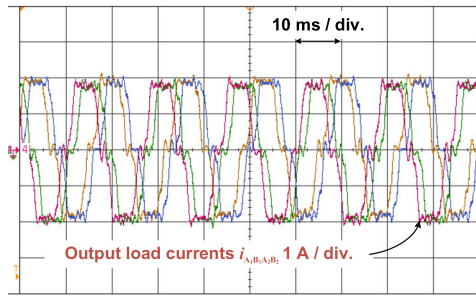

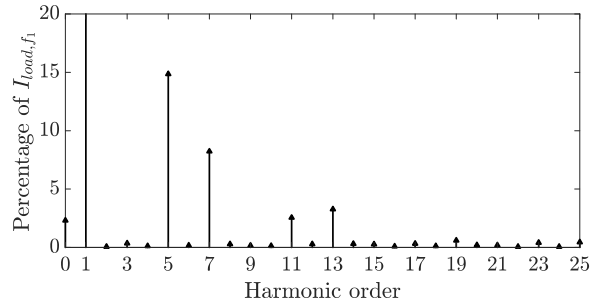(h) Capacitor current.

(i) Diode voltage and current.

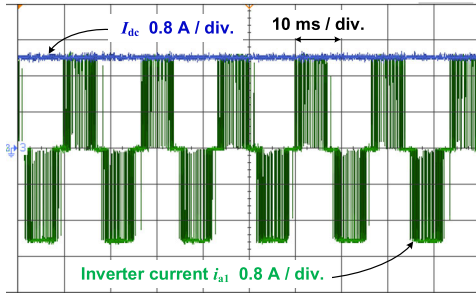(j) IGBT Switch voltage and current.

FIGURE 13. Experimental results of running the setup at $m = 1$.

(a) Load phase currents phases ($A_1, B_1, A_2,$ and B_2).

(b) Harmonic spectrum of the load current.

(c) Inverter output current and the dc-link current.

(d) Harmonic spectrum of the inverter current.
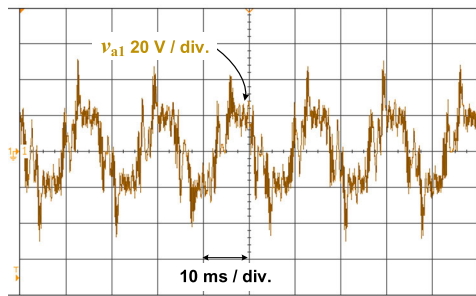
(e) Load phase voltage.

(f) Harmonic spectrum of the load voltage.

(g) Dc-link and inverter input Voltages.

(h) Capacitor current.

(i) Diode voltage and current.

(j) IGBT Switch voltage and current.

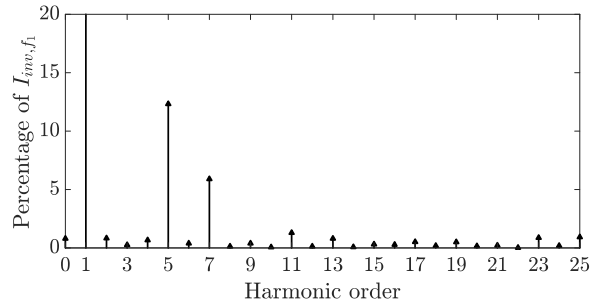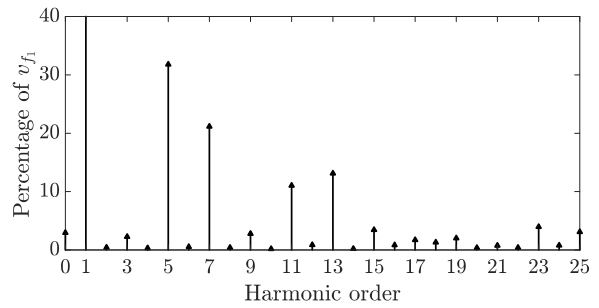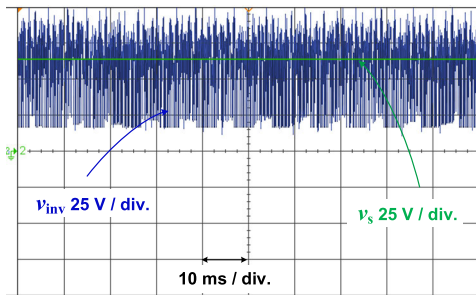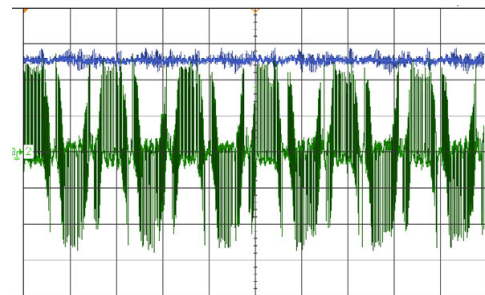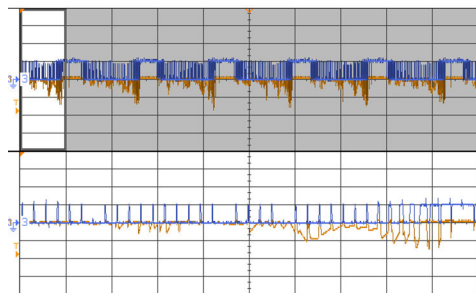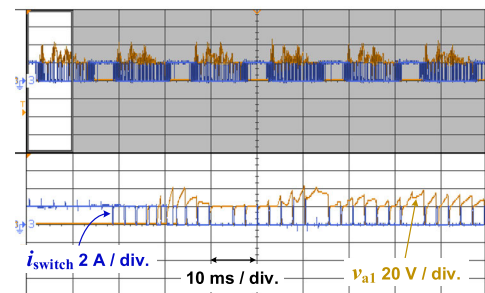**FIGURE 14.** Experimental results of running the setup at $m = 1.0773$.

TABLE 4. THD comparison between region I and II.

Modulation index	Variable	THD
$m = 1$	Load current	3.68%
	Inverter current	1.74%
	Load voltage	15.6%
$m = 1.0773$	Load current	16.88%
	Inverter current	14.14%
	Load voltage	37%

The capacitor current is shown in Fig. 13(g). It represents the filtered harmonics from the inverter output current as excepted.

The supply voltage V_{dc} and the inverter input voltage V_{inv} are shown in Fig. 13(h). From the inverter structure in Fig. 1, the inverter voltage is the summation of the two input voltages of the two three-phase inverters. Each input voltage is equal to the line voltage between the two activated phases due to the switching state applied to the inverter. The programmable supply applies a constant voltage at the required level to regulate the current and keep it at the set value. The currents and voltages of the series diode used to implement the C-CSI are shown in Fig. 13(i) and the purpose of the diode can be seen as it protects the IGBT/anti-parallel diode from reverse conducting due to negative voltages that might appear because of the nature of the load. The current and voltages of the switch are shown in Fig. 13(j) and it shows that the switch conducts pulsations between zero and the dc-link current values. The voltage on the other hand is subject to the loading condition and capacitor selection. It is expected to have higher instantaneous voltages because of the selection of small capacitors and that should be noted in the selection of the rating switches. The results of the C-CSI running in Region II are illustrated in Fig. 14. The waveforms of the output currents have a flat-top shape because of the injection as in Fig. 14(a). The cost of extending the modulation index appears in the harmonic spectrum of the load and inverter currents as in Fig. 14(b), (d).

The 5th and 7th harmonics are a bit higher in the load currents since the capacitor selected resonates with the load inductance at the 13th harmonic. However, the 17th and 19th harmonics are diminished because of that selection. The load voltage is shown in Fig. 14(e) and it can be noticed that the harmonics showing in the load current are amplified in the voltage spectrum in Fig. 14(f). Consequently, this phenomenon affects both the voltages before and after the inductor V_{dc} and V_{inv} as shown in Fig. 14(g), and the switches and diodes selection since higher voltage peaks are expected in addition to the increased voltage due to the extension in the first place as shown in Fig. 14(i) and (j).

The harmonics of the currents in Region II are analyzed by MATLAB to process the recorded data points of the waveforms. The formula for calculating the THD of the measured currents is defined in (14). The THD of the currents and voltage waveforms are illustrated in TABLE 4. As can be noticed,

the $m = 1.0773$ case has higher THD values compared to the $m = 1$ case.

$$\text{THD} = \frac{1}{I_{f1}}\sqrt{\sum_{l=2}^{30}\left(I_{fl}\right)^2} \tag{14}$$

where I_l is the harmonic current of the order l and I_1 is the fundamental current component.

V. CONCLUSION

This paper presents a new modulation scheme to control a six-phase C-CSI with minimized harmonic contents. The proposed method can also increase the modulation index range by about 8% which is attractive for motor drive applications that can lead to improving the torque density. The modulation index range is classified into two regions and the calculation of the dwell times is the same for the full range which can help with simple implementation. The experimental results show that the method is effective in eliminating the low-order harmonic in Region I where the degrees of freedom allow this feature. The extension of the modulation range is verified experimentally as well at the cost of an increase in the asymmetries harmonic content. The C-CSI topology combined with the proposed method is utilized to produce the output currents with unavoidable, yet minimized, harmonic content in the extension region with a near flat-top waveform. This feature is also required in motor drive applications to avoid iron saturation and exceeding designed current stresses for the converter semiconductors. The simplicity of the method promotes it for application to other multiphase systems easily based on their respective asymmetry subspaces.

REFERENCES

[1] E. Giraldo and A. Garces, "An adaptive control strategy for a wind energy conversion system based on PWM-CSC and PMSG," *IEEE Trans. Power Syst.*, vol. 29, no. 3, pp. 1446–1453, May 2014.

[2] M. Popat, B. Wu, F. Liu, and N. Zargari, "Coordinated control of cascaded current-source converter based offshore wind farm," *IEEE Trans. Sustain. Energy*, vol. 3, no. 3, pp. 557–565, Jul. 2012.

[3] D. Jovcic and J. V. Milanovic, "Offshore wind farm based on variable frequency mini-grids with multiterminal DC interconnection," in *Proc. 8th IEE Int. Conf. AC DC Power Transmiss. (ACDC)*, 2006, pp. 215–219.

[4] V. Madonna, G. Migliazza, P. Giangrande, E. Lorenzani, G. Buticchi, and M. Galea, "The rebirth of the current source inverter: Advantages for aerospace motor design," *IEEE Ind. Electron. Mag.*, vol. 13, no. 4, pp. 65–76, Dec. 2019.

[5] G.-J. Su and L. Tang, "Current source inverter based traction drive for EV battery charging applications," in *Proc. IEEE Vehicle Power Propuls. Conf.*, Sep. 2011, pp. 1–6.

[6] G.-J. Su, L. Tang, and Z. Wu, "Extended constant-torque and constant-power speed range control of permanent magnet machine using a current source inverter," in *Proc. IEEE Vehicle Power Propuls. Conf.*, Sep. 2009, pp. 109–115.

[7] Z. Wu and G.-J. Su, "High-performance permanent magnet machine drive for electric vehicle applications using a current source inverter," in *Proc. 34th Annu. Conf. IEEE Ind. Electron.*, Nov. 2008, pp. 2812–2817.

[8] F. Chen, H. Ding, S. Lee, W. Feng, T. M. Jahns, and B. Sarlioglu, "Current source inverter based large constant power speed ratio SPM machine drive for traction applications," in *Proc. IEEE Transp. Electrific. Conf. Expo (ITEC)*, Jun. 2020, pp. 216–221.

[9] Rockwell Automation. *Powerflex 7000 Medium Voltage AC Drives*. Accessed: Jan. 28, 2023. [Online]. Available: https://www.rockwellautomation.com/en-us/products/hardware/allen-bradley/drives/medium-voltage-ac-drives/powerflex-7000-ac-drive.html

[10] H.-C. Chen and H.-H. Huang, "Design of buck-type current source inverter fed brushless DC motor drive and its application to position sensorless control with square-wave current," *IET Electr. Power Appl.*, vol. 7, no. 5, pp. 416–426, May 2013.

[11] J. He, Y. Lyu, J. Han, and C. Wang, "An SVM approach for five-phase current source converters output current harmonics and common-mode voltage mitigation," *IEEE Trans. Ind. Electron.*, vol. 67, no. 7, pp. 5232–5245, Jul. 2020.

[12] Y. Xu, Z. Wang, P. Liu, and J. He, "A soft-switching current-source-inverter-fed motor drive with reduced common-mode voltage," *IEEE Trans. Ind. Electron.*, vol. 68, no. 4, pp. 3012–3021, Apr. 2021.

[13] F. Barrero and M. J. Duran, "Recent advances in the design, modeling, and control of multiphase machines—Part I," *IEEE Trans. Ind. Electron.*, vol. 63, no. 1, pp. 449–458, Jan. 2016.

[14] M. J. Duran and F. Barrero, "Recent advances in the design, modeling, and control of multiphase machines—Part II," *IEEE Trans. Ind. Electron.*, vol. 63, no. 1, pp. 459–468, Jan. 2016.

[15] M. Qiao, C. Jiang, Y. Zhu, and G. Li, "Research on design method and electromagnetic vibration of six-phase fractional-slot concentrated-winding PM motor suitable for ship propulsion," *IEEE Access*, vol. 4, pp. 8535–8543, 2016.

[16] L. P. Di Noia and R. Rizzo, "Design of a five-phase permanent-magnet motor for the electric steering of an aircraft nose landing gear," *IET Electr. Syst. Transp.*, vol. 7, no. 4, pp. 327–333, Dec. 2017.

[17] A. Salem and M. Narimani, "A review on multiphase drives for automotive traction applications," *IEEE Trans. Transport. Electrific.*, vol. 5, no. 4, pp. 1329–1348, Dec. 2019.

[18] W. N. W. A. Munim, M. J. Duran, H. S. Che, M. Bermúdez, I. G. Prieto, and N. A. Rahim, "A unified analysis of the fault tolerance capability in six-phase induction motor drives," *IEEE Trans. Power Electron.*, vol. 32, no. 10, pp. 7824–7836, Oct. 2017.

[19] K. S. Khan, W. M. Arshad, and S. Kanerva, "On performance figures of multiphase machines," in *Proc. 18th Int. Conf. Electr. Mach.*, Sep. 2008, pp. 1–5.

[20] P. Liu, Z. Wang, Q. Song, Y. Xu, and M. Cheng, "Optimized SVM and remedial control strategy for cascaded current-source-converters-based dual three-phase PMSM drives system," *IEEE Trans. Power Electron.*, vol. 35, no. 6, pp. 6153–6164, Jun. 2020.

[21] Y. Zhao and T. A. Lipo, "Space vector PWM control of dual three-phase induction machine using vector space decomposition," *IEEE Trans. Ind. Appl.*, vol. 31, no. 5, pp. 1100–1109, Sep. 1995.

[22] Y. Yu, L. Gao, Y. Liu, and F. Chai, "24-sector space vector decomposition for a dual three-phase PMSM," in *Proc. 17th Int. Conf. Electr. Mach. Syst. (ICEMS)*, Oct. 2014, pp. 1601–1606.

[23] W. Kun, Y. Xiaojie, W. Chenchen, and Z. Minglei, "An equivalent dual three-phase SVPWM realization of the modified 24-sector SVPWM strategy for asymmetrical dual stator induction machine," in *Proc. IEEE Energy Convers. Congr. Expo. (ECCE)*, Sep. 2016, pp. 1–7.

[24] K. Marouani, L. Baghli, D. Hadiouche, A. Kheloui, and A. Rezzoug, "A new PWM strategy based on a 24-sector vector space decomposition for a six-phase VSI-fed dual stator induction motor," *IEEE Trans. Ind. Electron.*, vol. 55, no. 5, pp. 1910–1920, May 2008.

[25] K. Marouani, L. Baghli, D. Hadiouche, A. Kheloui, and A. Rezzoug, "Discontinuous SVPWM techniques for double star induction motor drive control," in *Proc. 32nd Annu. Conf. IEEE Ind. Electron. (IECON)*, Nov. 2006, pp. 902–907.

[26] E. Levi, "Advances in converter control and innovative exploitation of additional degrees of freedom for multiphase machines," *IEEE Trans. Ind. Electron.*, vol. 63, no. 1, pp. 433–448, Jan. 2016.

[27] J. Prieto, F. Barrero, M. J. Durán, S. T. Marin, and M. A. Perales, "SVM procedure for *n*-phase VSI with low harmonic distortion in the overmodulation region," *IEEE Trans. Ind. Electron.*, vol. 61, no. 1, pp. 92–97, Jan. 2014.

[28] G. Carrasco and C. A. Silva, "Space vector PWM method for five-phase two-level VSI with minimum harmonic injection in the overmodulation region," *IEEE Trans. Ind. Electron.*, vol. 60, no. 5, pp. 2042–2053, May 2012.

[29] S. Paul and K. Basu, "Overmodulation techniques of asymmetrical six-phase machine with optimum harmonic voltage injection," *IEEE Trans. Ind. Electron.*, vol. 68, no. 6, pp. 4679–4690, Jun. 2021.

[30] N. A. Azeez, K. Gopakumar, J. Mathew, and C. Cecati, "A harmonic suppression scheme for open-end winding split-phase IM drive using capacitive filters for the full speed range," *IEEE Trans. Ind. Electron.*, vol. 61, no. 10, pp. 5213–5221, Oct. 2014.

[31] C. Zhou, G. Yang, and J. Su, "PWM strategy with minimum harmonic distortion for dual three-phase permanent-magnet synchronous motor drives operating in the overmodulation region," *IEEE Trans. Power Electron.*, vol. 31, no. 2, pp. 1367–1380, Feb. 2016.

[32] M. A. Elgenedy, A. A. Elserougi, A. S. Abdel-Khalik, A. M. Massoud, and S. Ahmed, "A space vector PWM scheme for five-phase current-source converters," *IEEE Trans. Ind. Electron.*, vol. 63, no. 1, pp. 562–573, Jan. 2016.

[33] Q. Wei, B. Wu, D. Xu, and N. R. Zargari, "A natural-sampling-based SVM scheme for current source converter with superior low-order harmonics performance," *IEEE Trans. Power Electron.*, vol. 31, no. 9, pp. 6144–6154, Sep. 2016.

[34] Y. Geng, R. Deng, W. Dong, K. Wang, H. Liu, and X. Wu, "An overlap-time compensation method for current-source space-vector PWM inverters," *IEEE Trans. Power Electron.*, vol. 33, no. 4, pp. 3192–3203, Apr. 2018.

[35] E. Levi, N. Bodo, O. Dordevic, and M. Jones, "Recent advances in power electronic converter control for multiphase drive systems," in *Proc. IEEE Workshop Electr. Mach. Design, Control Diagnosis (WEMDCD)*, Mar. 2013, pp. 158–167.

[36] G. Feng, C. Lai, M. Kelly, and N. C. Kar, "Dual three-phase PMSM torque modeling and maximum torque per peak current control through optimized harmonic current injection," *IEEE Trans. Ind. Electron.*, vol. 66, no. 5, pp. 3356–3368, May 2019.

[37] K. Wang, Z. Q. Zhu, Y. Ren, and G. Ombach, "Torque improvement of dual three-phase permanent-magnet machine with third-harmonic current injection," *IEEE Trans. Ind. Electron.*, vol. 62, no. 11, pp. 6833–6844, Nov. 2015.

[38] Y. Hu, Z. Q. Zhu, and M. Odavic, "Torque capability enhancement of dual three-phase PMSM drive with fifth and seventh current harmonics injection," *IEEE Trans. Ind. Appl.*, vol. 53, no. 5, pp. 4526–4535, Sep./Oct. 2017.

[39] F. Liu, B. Wu, M. Pande, and N. R. Zargari, "Zero-speed operation of high-power PWM current-source-inverter-fed induction motor drive," *IEEE Trans. Power Electron.*, vol. 27, no. 6, pp. 3020–3027, Jun. 2012.

AHMED SALEM (Graduate Student Member, IEEE) received the B.Sc. (Hons.) and M.Sc. degrees in electrical engineering from Alexandria University, Alexandria, Egypt, in 2014 and 2018, respectively, and the Ph.D. degree in electrical and computer engineering from McMaster University, Hamilton, ON, Canada, in 2022. He is on leave from working as an Assistant Lecturer (Tenure Track) with the Electrical Engineering Department, Alexandria University. He is currently a Drive Control Engineer at the Powertrain Systems Department, Valeo. During his Ph.D. studies, he was associated with the EECOMOBILITY CREATE/ORF Project working on the E-Motor side. His research interests include power electronics and electric drives in electrified transportation applications.

MEHDI NARIMANI (Senior Member, IEEE) received the Ph.D. degree in electrical engineering from the University of Western Ontario, London, ON, Canada, in 2012. He is currently an Assistant Professor with the Department of Electrical and Computer Engineering, McMaster University, Hamilton, ON, Canada. Prior to joining McMaster University, he was a Power Electronics Engineer with Rockwell Automation Canada, Cambridge, ON, Canada. He has authored/coauthored more than 90 journals and conference proceeding papers, coauthored a Wiley-IEEE Press book, and holds seven issued/pending U.S./European patents. His current research interests include power conversion, high-power converters, control of power electronics converters, fast EV chargers, and wireless EV charging systems.

• • •